Optics Letters

Polarization-insensitive high-numerical-aperture metalens for wide-field super-resolution imaging

Lieyu Chen,[1] Wenwei Liu,[1,4] Zhancheng Li,[1] Yuebian Zhang,[1] Hua Cheng,[1,5] Jianguo Tian,[1] and Shuqi Chen[1,2,3,6]

[1]The Key Laboratory of Weak Light Nonlinear Photonics, Ministry of Education, School of Physics and TEDA Institute of Applied Physics, Nankai University, Tianjin 300071, China
[2]School of Materials Science and Engineering, Smart Sensing Interdisciplinary Science Center, Nankai University, Tianjin 300350, China
[3]The Collaborative Innovation Center of Extreme Optics, Shanxi University, Taiyuan 030006, China
[4]wliu@nankai.edu.cn
[5]hcheng@nankai.edu.cn
[6]schen@nankai.edu.cn

Received 5 October 2023; revised 1 January 2024; accepted 21 February 2024; posted 23 February 2024; published 18 March 2024

The development of super-oscillatory lens (SOL) offers opportunities to realize far-field label-free super-resolution microscopy. Most microscopes based on a high numerical aperture (NA) SOL operate in the point-by-point scanning mode, resulting in a slow imaging speed. Here, we propose a high-NA metalens operating in the single-shot wide-field mode to achieve real-time super-resolution imaging. An optimization model based on the exhaustion algorithm and angular spectrum (AS) theory is developed for metalens design. We numerically demonstrate that the optimized metalens with an NA of 0.8 realizes the imaging resolution (imaging pixel size) about 0.85 times the Rayleigh criterion. The metalens can achieve super-resolution imaging of an object with over 200 pixels, which is one order of magnitude higher than the unoptimized metalens. Our method provides an avenue toward single-shot far-field label-free super-resolution imaging for applications such as real-time imaging of living cells and temporally moving particles.

https://doi.org/10.1364/OL.506612

The resolution of a conventional optical microscope is limited by the Rayleigh criterion ($R_c = 0.61\lambda/\mathrm{NA}$) [1], where λ and NA are the operating wavelength and numerical aperture, respectively. Over the past decades, great efforts have been devoted to overcoming the fundamental limitation on the resolution of microscopes, and various super-resolution technologies have been developed. These technologies can be categorized into three broad groups: near-field [2], far-field fluorescence-based [3], and far-field label-free microscopies [4–6]. The first two technologies rely on either complex near-field operations or specimen preprocesses. In contrast, the far-field label-free technique overcomes the above problems, which is non-contact and noninvasive.

One of the most promising far-field label-free microscopy technologies is based on wavefront modulation. Toraldo suggested that the resolving ability of an imaging system could be improved using a pupil filter [7]. Berry then proposed the concept of optical super-oscillation, which helps to explain the mechanism of super-resolution pupil filters [8]. Recently, there has been a growing interest in developing far-field label-free super-resolution microscopy based on a high-NA super-oscillation lens (SOL) [5,6] achieved through phase or amplitude elements. The focal spot of an SOL could be smaller than the super-oscillation criterion of $0.38\lambda/\mathrm{NA}$ and could theoretically reach infinitesimal with severe sidelobes [9,10]. Such a super-oscillation spot is also limited by the field of view (FOV) with large sidebands around the focus, which is usually applied to scanning super-oscillatory imaging [5]. Single-shot super-oscillatory imaging with an extended FOV can significantly improve the imaging speed [11]. Recently, thanks to the rapid exploitation of metasurfaces for efficient wavefront control [12], the development of high-performance super-oscillatory metalens (SOM) becomes possible [13,14]. Achromatic [15] and wide-angle [16] SOMs have also been reported. However, most reported SOMs for single-shot super-resolution imaging still suffer from an extremely limited FOV or low NA, which is not suitable for real-time super-resolution imaging. Owing to the prevalence of severe off-axis aberrations for high-NA metalenses, how to improve the imaging performance of SOMs remains a question.

Here, we proposed a polarization-insensitive dielectric SOM with an NA of 0.8 for single-shot wide-field super-resolution imaging. For the metalens design, an optimization model based on the exhaustive algorithm and angular spectrum (AS) theory was developed. The model could balance the spot size, peak intensity (PI), and sidelobe ratio (SR, defined as the ratio of the maximum sidelobe intensity to the central lobe peak intensity) of the point spread function (PSF) of the metalens. Then the off-axis PSF performance of the proposed SOM was numerically verified with the finite-difference time-domain (FDTD) method. In addition, the resolution of the SOM is close to $0.85R_c$ in a wide FOV of 10λ.

The metalens consists of an array of amorphous silicon (a-Si) nanopillars with different diameters arranged in a hexagonal lattice on a SiO_2 substrate to increase the duty ratio [Figs. 1(a) and 1(b)]. The numerical simulations of the nanopillars were

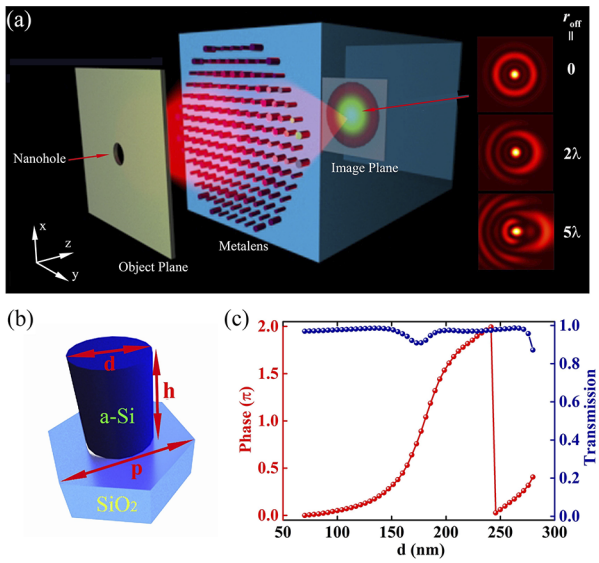

Fig. 1. (a) Schematic of the SOM for super-resolution imaging. Insets: images of the nanohole with different off-axis displacements. (b) Metalens consists of a-Si nanopillars arranged in a hexagonal lattice, where p, h, and d are the lattice size, height, and diameter of the nanopillar, respectively. (c) Simulated transmission intensity and phase as a function of the diameter of nanopillar.

performed with Lumerical FDTD software. The refractive indices of the nanopillars and the substrate at the operating wavelength of 850 nm are set as 3.6 and 1.45 [17], respectively. The lattice size and height of the nanopillars are $p = 500$ nm and $h = 560$ nm. To achieve super-resolution imaging with a wide FOV, we start from the PSF of the SOM, which can be characterized by the image of a subwavelength nanohole with an off-axis displacement r_{off} [Fig. 1(a)]. The nanohole locates in front of the metalens with a high NA, and the image plane locates in the substrate corresponding to a low NA compared with that in the object space. The phase of a nanopillar can be controlled when varying the diameter d, and a 0–2π phase coverage with intensity transmission over 90% is achieved [Fig. 1(c)].

Generally, the ideal phase distribution of focusing should be further adjusted to generate a local super-resolution intensity distribution and a modified FOV. The phase profile of the proposed SOM can be expressed as

$$\varphi_{SOM}(r) = \varphi_{ord}(r) + \varphi_{opt}(r), \tag{1}$$

where $r = \sqrt{x^2 + y^2}$ is the distance from an arbitrary position $P(x,y)$ of the metalens to its central position, $\varphi_{ord}(r)$ is the phase profile of the ordinary metalens, and $\varphi_{opt}(r)$ is the additional optimized binary phase profile. Such binary setup significantly reduces computation cost in the optimization and provides sufficient flexibility of wavefront manipulation. Instead of a conventional hyperbolic phase profile for focusing [18], the phase profile of the ordinary metalens could be written as Eq. (2) to ensure a constructive interference at the designed image plane while an on-axis point object is imaged:

$$\varphi_{ord}(r) = \frac{2\pi}{\lambda}\left[n_1\left(l_1 - \sqrt{r^2 + l_1^2}\right) + n_2\left(l_2 - \sqrt{r^2 + l_2^2}\right)\right], \tag{2}$$

where l_1 and l_2 are the object and image distances and $n_1 = 1$ and $n_2 = 1.45$ are the refractive indices in the object and image

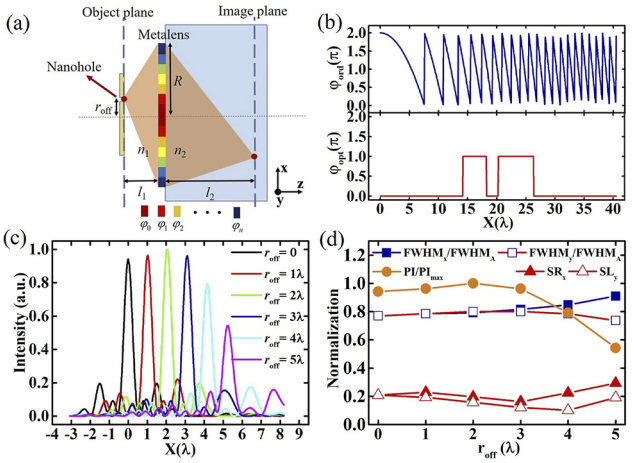

Fig. 2. (a) Schematic of the super-resolution imaging process. (b) Phase profile of the ordinary metalens (blue line) and the optimized binary phase profile (red line) along the radial direction. (c) x-cut lines of the theoretical off-axis PSF. (d) PI/PI$_{max}$, FWHM/FWHM$_A$, and SR of the theoretical PSF for the off-axis displacements from 0 to 5λ. FWHM$_A$ is the diffraction-limited Airy spot size.

spaces, respectively. Specifically, the radius of the metalens is set as $R = 40\lambda$, and the NAs in the object and image spaces are set as $NA_1 = 0.8$ and $NA_2 = 0.08$ [Fig. 2(a)]. Accordingly, $l_1 = 30\lambda$ and $l_2 = 723.9\lambda$ are obtained from $l_2 = R/\tan(\text{asin}(NA_i/n_i))$. Such a metalens with phase distribution of $\varphi_{ord}(r)$ still suffers from severe off-axis aberrations, leading to an extremely limited FOV in imaging. The wavefront diffracted from the nanohole with a diameter of 0.6λ is almost equivalent to the spherical wavefront. According to the AS theory, the PSF of the system under unpolarized incidence can be described as

$$I(x_{off}, y_{off}; x, y) = \left|\int\int_{-\infty}^{\infty} A(f_x, f_y) e^{i2\pi(f_x x + f_y y + f_z l_2)} df_x df_y\right|^2, \tag{3}$$

where $f_x, f_y, f_z = \sqrt{1/\lambda^2 - f_x^2 - f_y^2}$ are the frequency components along x-, y-, and z-directions and $A(f_x, f_y)$ is the angular spectra of the light fields near the light-emergent surface of the metalens, which can be calculated through

$$\begin{aligned} A(f_x, f_y) &= \int\int_{-\infty}^{\infty} U(x,y)t(r)e^{-i2\pi(f_x x + f_y y)} dx dy \\ &= \mathrm{F}[U(x,y)t(r)e^{-i2\pi(f_x x + f_y y)}], \end{aligned} \tag{4}$$

where $U(x,y) \approx u_0 e^{i2\pi n_1 l_r/\lambda}/l_r$ is the spherical wavefront of the off-axis point, $l_r = \sqrt{(x - x_{off})^2 + (y - y_{off})^2 + l_1^2}$ is the distance between the off-axis point (x_{off}, y_{off}) in the object plane and the point $P(x,y)$ of the metalens, and $t(r) \approx \text{circ}(r/R)e^{i\varphi_{SOM}}/l_r$ is the transmission function of the SOM. The spatial coordinates of the PSF are transformed through a fixed magnification into the ones that characterize the actual size of the object.

In the design of the SOM with a high NA for wide-field super-resolution imaging, the optimization process of the binary phase (0, π) takes both the performance improvement of off-axis aberration and resolution into account. We first binarize $\varphi_{opt}(r)$ into 20 rings. Since the phase value of each annular ring is independent of each other, we build a library consisting of 2^{20} kinds of additional binary phase profiles and use the exhaustion algorithm and AS theory in the optimization. We propose a multiple constrained optimization model for the optimizing selections from

the binary phase library, which includes constraints of the PI, full width at half maximum (FWHM), and SR of the PSFs. The corresponding off-axis PSFs are calculated using Eqs. (3) and (4). The objective function f_{obj} is defined as Eq. (5a) for off-axis aberration compensation. The size of the binary phase library (start at 2^{20}) greatly decreases when starting from $r_{\mathrm{off}}=0$ with symmetry in x- and y-directions. The mathematical expression of this model can be expressed as

$$f_{\mathrm{obj}} = \max \mathrm{PI}(r_{\mathrm{off}} = 5\lambda) \tag{5a}$$

$$\text{s.t. } \mathrm{FWHM}_{x,y}(r_{\mathrm{off}} = 0, 5\lambda) < 0.9\mathrm{FWHM}_{\mathrm{A}} \tag{5b}$$

$$\mathrm{SR}_{x,y}(r_{\mathrm{off}} = 0, 5\lambda) < 0.25 \tag{5c}$$

$$\mathrm{PI}(r_{\mathrm{off}} = 5\lambda)/\mathrm{PI}(r_{\mathrm{off}} = 0\lambda) > 0.6 \tag{5d}$$

$$\varphi_{\mathrm{opt}}(r_i) \in \{0, \pi\},\ i = 1, 2, \cdots 20, \tag{5e}$$

where $\mathrm{FWHM}_{\mathrm{A}} = 0.51\lambda/\mathrm{NA}$ is the spot size of the PSF (Airy disk) of a conventional lens and r_i is the radius of the i-th annular ring of the phase profile. Note that the proposed SOM does not exactly break the spatial frequency limit that can transmit in the optical system.

The optimized binary phase $\varphi_{\mathrm{opt}}(r)$ is obtained in Fig. 2(b), resulting in compensated off-axis aberrations within an extended FOV. We investigated the performance of the theoretical PSF of the designed SOM using the AS method. Figure 2(c) shows the x-cut lines of the PSF for the r_{off} ranging from 0 to 5λ. Figure 2(d) shows the $\mathrm{PI/PI_{max}}$, $\mathrm{FWHM/FWHM_A}$, and SR of the PSF as functions of r_{off}, where $\mathrm{PI_{max}}$ is the maximum PI. Note that the $\mathrm{PI/PI_{max}}$ of the imaging spot remains larger than 54% while keeping r_{off} smaller than 5λ to ensure acceptable imaging quality. The FWHM of different imaging spots remains below 0.58λ, smaller than the diffraction limit of 0.64λ. The calculated SR is smaller than 30% in the working FOV, indicating significant suppression of sidelobes.

To characterize the imaging performance of the designed SOM, we simulated the imaging of the subwavelength nanohole by FDTD and AS methods. Perfectly matched layer (PML) boundary condition is employed in the z-direction. First, the simulated results of the transmission function in the x- and y-directions of the metalens under x- and y-polarized incidence were obtained by the FDTD method. Then, the PSF of the metalens under unpolarized incidence could be calculated by the incoherently superposition of the PSF under x- and y-polarized incidence by the AS method using MATLAB. For the ordinary metalens, although the PSF for $r_{\mathrm{off}}=0$ is an Airy spot, the off-axis aberrations become significant when slightly increasing the r_{off} [Fig. 3(a)]. In contrast, the size of the PSF of the SOM maintains smaller than that of the Airy spot for the r_{off} from 0 to 5λ at a cost of increasing sidelobes, and the off-axis aberrations are compensated [Fig. 3(b)]. The x- and y-cut-line intensity profiles of the PSFs for the ordinary metalens and SOM are shown in Figs. 3(c) and 3(d). Compared with the ordinary metalens, which suffers from a severe asymmetry of the intensity distribution in the x- and y-directions due to the off-axis aberrations, the intensity distributions of the designed SOM are more uniform with similar FWHMs for different r_{off} of the nanohole.

Figure 4(a) shows the x-cut-line intensity profiles of the off-axis PSF of the SOM, which is consistent with the calculated ones in Fig. 2(c) using the AS method. We simulated $\mathrm{PI/PI_{max}}$, $\mathrm{FWHM/FWHM_A}$, and SR of the PSF of the SOM as a function of r_{off} in Fig. 4(b). The $\mathrm{PI/PI_{max}}$ at an r_{off} smaller than 5λ remains larger than 52%. The spot sizes in the x- and y-directions, i.e.,

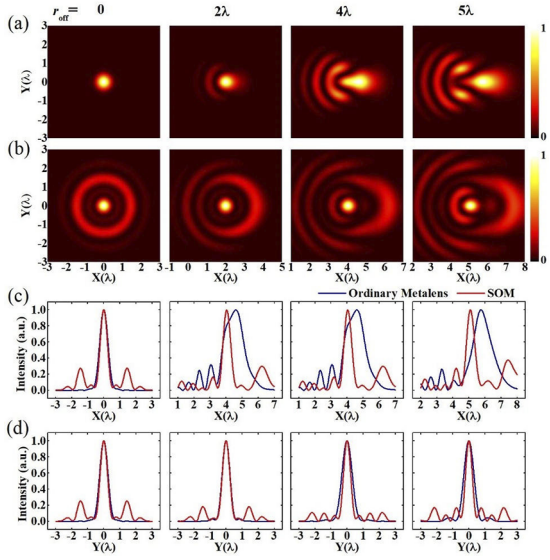

Fig. 3. Comparison between the simulated PSFs of the (a) ordinary metalens and (b) SOM for the off-axis displacements from 0 to 5λ. The corresponding (c) x-cut lines and (d) y-cut lines of the PSF for different off-axis displacements.

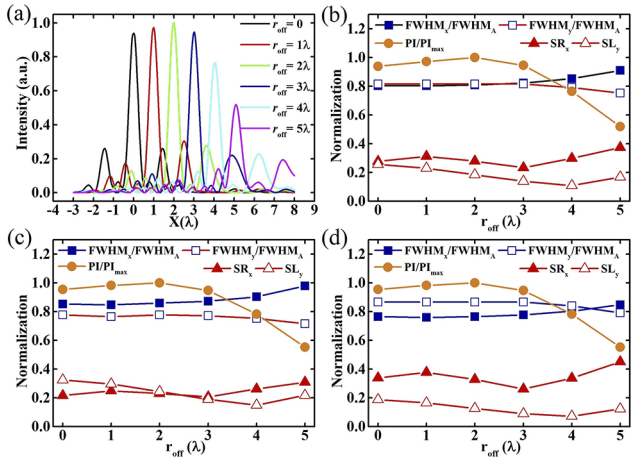

Fig. 4. (a) x-cut lines of the simulated off-axis PSF. The $\mathrm{PI/PI_{max}}$, $\mathrm{FWHM/FWHM_A}$ and SR of the PSF for the off-axis displacements from 0 to 5λ under (b) unpolarized and (c) x- and (d) y-polarized incidence. $\mathrm{FWHM_A}$ is the diffraction-limited Airy spot size.

FWHM_x and FWHM_y, remain about 0.52λ for the r_{off} from 0λ to 3λ, which is $0.83\mathrm{FWHM_A}$. The simulated maximum FWHM is about 0.58λ for r_{off} in the range from 3λ to 5λ, which is $0.93\mathrm{FWHM_A}$. The simulated SRs are slightly larger than those of the calculated ones in Fig. 2(d). Such discrepancy can be attributed to the effect of the near-field coupling between the nanopillars.

Normally, a conventional high-NA lens under linearly polarized incidence generates an asymmetric focal spot caused by optical transmission [19], which means that such a lens is polarization sensitive. However, the anisotropy of the central lobe of SOM spots is too small to show up. The proposed metalens under linearly polarized incidence can produce a nearly circularly symmetric spot at $r_{\mathrm{off}} < 5\lambda$, which means that such a metalens is polarization insensitive within certain limits. As

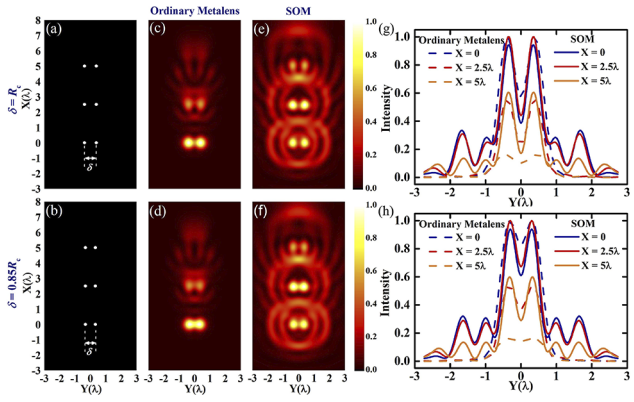

Fig. 5. Images of double-nanoholes in a metallic film. The center-to-center distances of the two adjacent nanoholes are (a) R_c and (b) $0.85R_c$. (c)–(f) Simulated images for (c),(d) the ordinary metalens and (e),(f) the SOM corresponding to panels (a),(b). (g) and (h) Comparison among the x-cut lines of the imaging intensity distributions for panels (a),(b).

shown in Figs. 4(c) and 4(d), there is a negligible difference in the spot sizes between the x- and y-directions for an off-axis displacement from 0 to 5λ under x-and y-polarized incidence, respectively.

To investigate the off-axis imaging performance and the resolving ability of the designed SOM, we simulated the imaging of the two test targets with unpolarized illumination. Each target consists of three double-nanoholes with the same center-to-center distance δ in a film [Figs. 5(a) and 5(b)]. The center of the bottom, middle, and top double-nanoholes locates at $x=0$ (the optical axis), 2.5λ, and 5λ, respectively. The distance δ for the first and second test targets are set as R_c and $0.85R_c$ ($R_c=0.763\lambda$). The imaging distribution is the resultant intensity distribution incoherently superposed by the intensity patterns of each single nanohole in the test target. As shown in Fig. 5(c), although the double-nanohole for $x=0$ can be resolved when using the ordinary metalens for imaging, the image suffers from apparent off-axis aberrations for $x=2.5\lambda$ and 5λ. When δ decreases to $0.85R_c$, the images of each double-nanoholes become blurry and the two spots merge into one, demonstrating that the ordinary metalens cannot be used for sub-diffraction imaging anymore [Fig. 5(d)]. Therefore, the resolution of the ordinary metalens is about R_c with an extremely limited FOV. In contrast, all of the double-nanoholes can be resolved by the SOM with negligible aberrations [Figs. 5(e) and 5(f)]. The comparison among the x-cut-line intensity patterns for each double-nanoholes in the first and second targets is shown in Figs. 5(g) and 5(h), respectively. Generally, the contrast defined in the Rayleigh criterion for distinguishing two adjacent points is 20% [20]. When using the SOM to image the double-nanoholes, the intensity contrasts corresponding to the double-nanoholes located at $x=0\lambda$, 2.5λ, and 5λ are 21%, 20%, and 35%, respectively, which can reach the distinguishing criterion. The resolution of the SOM keeps approximately $0.85R_c$ in an extended FOV of 10λ.

In summary, we propose a high-NA SOM to achieve wide-field super-resolution imaging under unpolarized incidence. Owing to the requirement for multi-parameters in a realistic imaging system, such as NA, FOV, and spatial resolution, a trade-off among these quantities is made in the optimization of the SOM. The PSF performance of the proposed metalens is verified through FDTD simulation, whose results are consistent with the theoretical ones. The designed SOM with an NA of 0.8 can achieve single-shot super-resolution imaging with the spatial resolution of about $0.85R_c$ within an extended FOV of 10λ, which includes more than 200 pixels. The amount of pixels is calculated by the number of pixels contained in the FOV. Our method provides a simple way to achieve far-field label-free super-resolution imaging with an improved FOV, which can potentially be applied in microscopy and bio-imaging such as the real-time imaging of living cells. The working wavelength of the SOM could also be extended to other wavelengths, which requires nanostructures with proper materials possessing high refractive indices or high conductivity.

Funding. National Key Research and Development Program of China (2021YFA1400601, 2022YFA1404501); National Natural Science Fund for Distinguished Young Scholar (11925403); National Natural Science Foundation of China (12122406, 12192253, 12274237, 12274239, U22A20258); Natural Science Foundation of Tianjin City (22JCYBJC00800, 22JCYBJC01350, 22JCZDJC00400).

Disclosures. The authors declare no conflicts of interest.

Data availability. The data that support the findings of this study are available from the authors upon reasonable request.

REFERENCES

1. L. Rayleigh, Phil. Mag. Ser. **8**, 477 (1879).
2. E. Betzig, J. K. Trautman, T. D. Harris, *et al.*, Science **251**, 1468 (1991).
3. E. Betzig, G. H. Patterson, R. Sougrat, *et al.*, Science **313**, 1642 (2006).
4. E. Narimanov, Adv. Photonics **1**, 1 (2019).
5. E. T. F. Rogers, J. Lindberg, T. Roy, *et al.*, Nat. Mater. **11**, 432 (2012).
6. F. Qin, K. Huang, J. Wu, *et al.*, Adv. Mater. **29**, 1602721 (2017).
7. G. T. Di Francia, Nuovo Cimento **9**, 426 (1952).
8. M. V. Berry and S. Popescu, J. Phys. A: Math. Gen. **39**, 6965 (2006).
9. K. Huang, H. Ye, J. Teng, *et al.*, Laser Photonics Rev. **8**, 152 (2014).
10. K. S. Rogers, K. N. Bourdakos, G. Yuan, *et al.*, Opt. Express **26**, 8095 (2018).
11. H. Yang, Y. Liu, and G. V. Eleftheriades, APL Photonics **8**, 056103 (2023).
12. S. Chen, W. Liu, Z. Li, *et al.*, Adv. Mater. **32**, 1805912 (2020).
13. Q. Zhang, F. Dong, H. Li, *et al.*, Adv. Opt. Mater. **8**, 1901885 (2020).
14. J. Zhou, Y. Zhou, F. Dong, *et al.*, Opt. Laser Technol. **161**, 109121 (2023).
15. Z. Li, T. Zhang, Y. Wang, *et al.*, Laser Photonics Rev. **12**, 1800064 (2018).
16. Z. Li, C. Wang, Y. Wang, *et al.*, Opt. Express **29**, 9991 (2021).
17. A. Arbabi, E. Arbabi, S. M. Kamali, *et al.*, Nat. Commun. **7**, 13682 (2016).
18. K. Huang, F. Qin, H. Liu, *et al.*, Adv. Mater. **30**, 1704556 (2018).
19. R. Dorn, S. Quabis, and G. Leuchs, J. Mod. Opt. **50**, 1917 (2003).
20. M. Born and E. Wolf, *Principles of Optics* (Cambridge, 1999).